

Photocatalytic Enhancements to the Reduction of 4-Nitrophenol by Resonantly Excited Triangular Gold–Copper Nanostructures

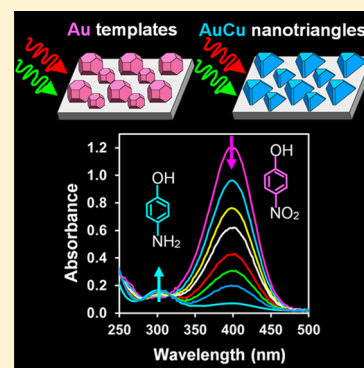
Maryam Hajfathalian,[†] Kyle D. Gilroy,[†] Ali Yaghoobzade,[†] Aarthi Sundar,[†] Teng Tan,[‡] Robert A. Hughes,[†] and Svetlana Neretina^{*,†}

[†]College of Engineering, Temple University, Philadelphia, Pennsylvania 19122, United States

[‡]Department of Physics, Temple University, Philadelphia, Pennsylvania 19122, United States

S Supporting Information

ABSTRACT: The reduction of 4-nitrophenol to 4-aminophenol by sodium borohydride serves as a well-established model reaction for assessing the catalytic activity of metal nanoparticles. While many of the studied nanoparticles are plasmonic in nature, there is little understanding of whether significant photocatalytic enhancements to the reaction rate are achievable. Here, we assess the catalytic and photocatalytic properties of highly faceted, substrate-immobilized nanoprism-like AuCu structures synthesized using a vapor phase templated-assembly technique. The so-formed structures have a bimetallic composition which is well-recognized for its catalytic capabilities as well as a strong localized surface plasmon resonance in the visible spectrum which gives rise to enhanced near-fields at the tips of the triangle. Using a dip catalyst modality, the structures are demonstrated as heterogeneous photocatalysts with a 32-fold enhancement to the reaction rate constant when resonantly illuminated with 10 mW/cm² laser light. The study demonstrates the potential of such structures as photocatalysts and validates the reduction of 4-nitrophenol as a reaction useful in assessing the photocatalytic capabilities of plasmonic nanostructures.



1. INTRODUCTION

The focus of metal nanostructure synthesis is increasingly shifting toward bimetallic systems.^{1,2} This activity is being spurred on by demonstrations of advanced functionalities in the areas of catalysis,^{3–6} plasmonics,^{7,8} and magnetism.⁹ It originates from the increased synthetic flexibility inherent to multicomponent systems as well as the ability to tune nanostructure properties by varying the relative proportions of the two metals. In this regard, catalytic nanostructures consisting of alloyed combinations of Au and Cu present one of the most promising bimetallic systems.¹⁰ Individually, both Au and Cu are well-established catalytic materials.^{11,12} The alloyed combination, however, offers potential from the standpoints of increased catalytic activity, greater selectivity, and, for the case of photocatalysis, the ability to tune the localized surface plasmon resonance (LSPR) to achieve optimal performance. AuCu nanostructures also offer higher resistance to oxidation when compared to structures comprised of elemental Cu, a property which could greatly increase catalyst lifetime. Early demonstrations of AuCu nanostructures as catalysts showed their effectiveness in the hydrogenation of dimethylxalate to methyl glycolate¹³ and in the oxidation of carbon monoxide,^{14,15} benzyl alcohol,¹⁶ and propene.¹⁷ More recent breakthroughs include: (i) the use of pentacle AuCu nanocrystals to achieve impressive catalytic performance for the model catalytic reaction which reduces 4-nitrophenol (4-NP) to 4-aminophenol (4-AP) by sodium borohydride,⁴ (ii) CO₂ electroreduction using Au₃Cu nanocubes,¹⁸ and (iii) the formation of methane through the reduction of carbon dioxide

by water in the presence of sunlight,³ a reaction which has the potential to transform a greenhouse gas back into a useable fuel.¹⁹

From the standpoint of AuCu nanostructure synthesis, much emphasis has been placed on forming nanostructures in a size regime where catalysis is most pronounced (i.e., < 15 nm).^{3,13–15,17,20–25} Such structures typically have spherical or near-spherical morphologies. Less studied are structures formed on larger length-scales where complex geometries and greater morphological control are more readily realizable.^{4,18,26–29} When structures are formed on length-scales greater than 50 nm they are generally considered less suitable for catalysis due to their low surface-area-to-volume ratio, but where notable exceptions occur.^{4,30} It is, however, in this size regime where the plasmonic properties are most easily tuned by varying the size, shape, and composition of the nanostructures. For the case of plasmonic photocatalysis,^{31–34} there is less certainty regarding the optimum nanostructure length-scale since a compromise must be formed between structures offering large surface-area-to-volume ratios and those offering plasmonic resonances which promote catalytic activity.

In previous studies, we have demonstrated a template-mediated assembly route in which substrate-immobilized Au nanostructures are exposed to the vapor arriving from a slowly sublimating foil of a second metal held in close proximity.^{35–38}

Received: May 13, 2015

Revised: June 25, 2015

Published: July 2, 2015

The processing temperature is chosen such that heterogeneous nucleation at the Au nanostructure is permissible while homogeneous nucleation is forbidden. As a consequence, the composition and shape of the Au nanostructures can be fundamentally altered while inhibiting the formation of new nanostructures elsewhere on the substrate. Of specific relevance to the current study is the demonstration that truncated Au octahedrons can be transformed into alloyed AuAg triangular nanostructures entirely comprised of (111) facets.³⁵ Such structures are valued for the intense plasmonic near-fields formed at the triangle tips.³⁹ Here, we adapt this directed assembly route to the AuCu system to form similarly shaped structures, but where smaller well-defined (100) and (110) facets are also present. Structures with this modified geometry are then assessed as catalysts and photocatalysts in the reduction of 4-NP. Observed is a 32-fold enhancement in the reaction rate constant when these structures are excited with light at a wavelength resonant with the LSPR.

2. RESULTS AND DISCUSSION

Figure 1 shows the synthetic scheme used to transform substrate-based Au templates into triangular AuCu nanostructures.

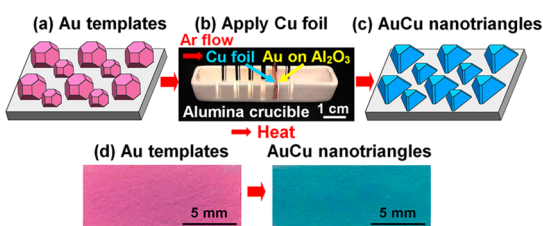


Figure 1. Synthetic scheme used to form triangular AuCu nanostructures. (a) The substrate-immobilized Au templates and (b) a Cu foil are placed into adjacent slits cut into an alumina crucible where at elevated temperatures they transform into (c) alloyed triangular AuCu nanostructures. (d) Optical images showing the color change which occurs as the templates are transformed into triangular nanostructures.

tures. The Au templates used in this assembly process (Figure 1a) are formed through the solid state dewetting⁴⁰ of 12 nm thick sputter deposited Au films onto (0001)-oriented sapphire substrates.⁴¹ The substrate and a Cu foil, both identical in size, are then placed into slots cut into an alumina crucible which maintains a separation distance of 0.5 mm (Figure 1b). The loaded crucible is then inserted into a tube furnace with flowing Ar and heated to a temperature of 885 °C for time intervals

lasting up to 24 h. This heating regimen allows Cu to sublimate from the foil, encounter weakly faceted Au truncated octahedrons which, through a combination of heterogeneous nucleation and solid state diffusion, transform into alloyed triangular AuCu nanostructures (Figure 1c). This morphological and compositional transformation is accompanied by a color change from pink to blue (Figure 1d). It is noted that structures produced in this manner are free of the ligands which can inhibit catalytic activity^{42,43} and may result in deviations from first order kinetics.⁴⁴

The morphological transformation which occurs during the assembly process was assessed using scanning electron microscopy (SEM). Figure 2a shows SEM images of the Au templates as well as a histogram of their diameters. The templates, which form at random positions over the surface of the substrate with an areal density of $3 \times 10^9 \text{ cm}^{-2}$, have an average diameter of 80 nm. The insets show weak faceting consistent with a [111]-oriented truncated octahedron bound by eight (111) and six (100) facets. This so-called Wulff shape represents the equilibrium configuration for a face centered cubic (fcc) crystal structure.⁴⁵ Figure 2b shows SEM images of identical templates after being subjected to a Cu vapor for 15 h. This process results in a nanostructure with three distinct types of facets, the most prominent of which are the four (111) facets which give rise to the nanoprism-like geometry. The three facets which dull the corners of the triangle are consistent with (100) faceting. The third facet-type, which connects the (111) side-facets to the top facet, is consistent with (110) faceting. It is noted that, while (110) facets are not typically observed for fcc metals, they have been identified as a part of the equilibrium crystal shape of Cu microstructures formed using solid state dewetting.⁴⁶ The uptake of Cu by the templates inevitably leads to larger structures, as is indicated by the histogram which shows an average triangle edge length of 160 nm. When templates are subjected to a Cu vapor for much shorter (5 h) or longer (24 h) durations the result is less desirable, yielding a mixture of hemispherical and triangular geometries. When optimal conditions are employed the triangular AuCu nanostructures are produced with a yield near 85%. They form two dominant epitaxial relationships with the substrate as is indicated by the fact that they predominantly point up or down in Figure 2b. This 180° difference in the in-plane orientation of epitaxially formed [111] structures, which arises from opposite stacking orders (i.e., ABCABC... and CBACBA...),³⁵ is a common occurrence for fcc metals.

The crystallographic orientation and composition of the triangular AuCu nanostructures were characterized using X-ray

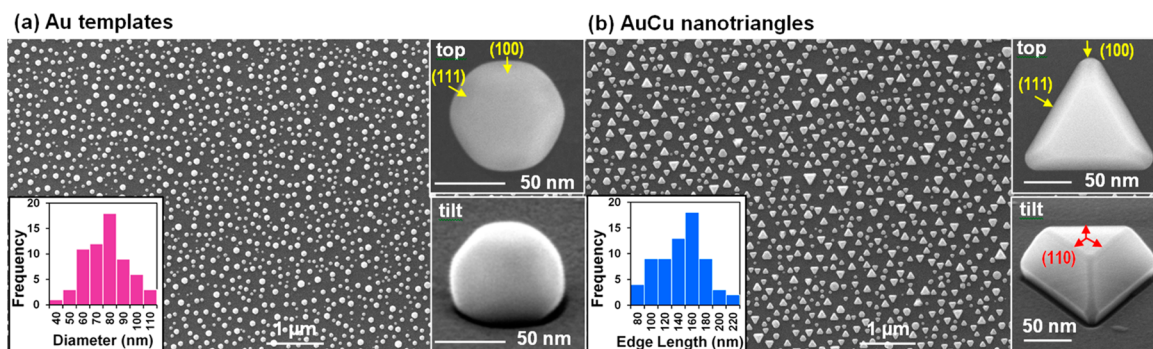


Figure 2. SEM images of (a) Au templates and (b) triangular AuCu nanostructures along with insets showing high resolution images of individual structures taken from a top- and a side-view. The histograms show the distribution of template diameters and triangle edge lengths.

diffraction (XRD) and energy-dispersive X-ray spectroscopy (EDS). Figure 3a shows the $\theta-2\theta$ XRD scans for both the Au

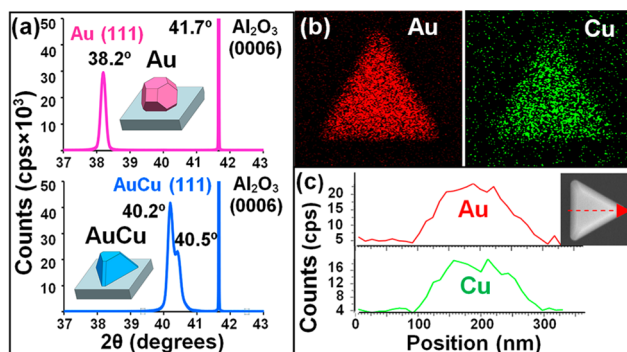


Figure 3. (a) $\theta-2\theta$ XRD scans on the Au templates and triangular AuCu nanostructures. (b) EDS elemental maps and (c) line-scans for triangular AuCu nanostructures.

templates and triangular AuCu nanostructures. The templates show a single reflection at 38.2° which is expected for Au structures with a [111]-orientation normal to the substrate. The 15 h assembly process results in the complete elimination of the (111) Au reflection. It is replaced with a highly reproducible split peak with maxima at 40.2° and 40.5°. This splitting could indicate that the structures are in the very early stages of transforming from an alloy to an intermetallic. The Au–Cu binary phase diagram shows a phase transition near 400 °C from a disordered fcc alloy to a tetragonal crystal structure with alternating planes of Au and Cu atoms along the [001]-

direction. Such transitions are, however, quite slow, requiring several months of annealing for bulk samples.⁴⁷ Even if this is the case, these structures are more accurately described as alloys since the ratio of the lattice constants of 0.99 is far from the 0.935 value expected for the ordered phase. Alternatively, the split peaks could indicate a nonuniformity originating from different size structures tending toward different equilibrium concentrations. In such a scenario, an Au–Cu solid solution, with alloy lattice constants varying linearly between the Au and Cu values, yields compositions of Au_{0.56}Cu_{0.44} and Au_{0.50}Cu_{0.50} for the two peaks. The fact that the (111) AuCu reflection is higher in intensity than the same reflection exhibited by Au template stems from the greater volume associated with the triangular structure. On the basis of this XRD data and the observed AuCu faceting relative to a substrate alignment flat, the two dominant crystallographic orientation relationships for the triangular structures are assigned as (111)[$\bar{2}11$]-AuCu|| (0001)[11 $\bar{2}$]sapphire and (111)[$\bar{2}\bar{1}\bar{1}$]-AuCu|| (0001)[11 $\bar{2}$]sapphire. Consistent with the X-ray data are the EDS line-scans and elemental maps (Figure 3b) which show uniform alloying with a composition near Au_{0.5}Cu_{0.5}.

The transformation of the Au templates to triangular AuCu nanostructures resulted in dramatic changes to the optical properties as is indicated by the images shown in Figure 1d. The optical extinction spectra of the structures, shown in Figure 4a, show that the transformation gives rise to both a large shift in the LSPR peak from 560 to 640 nm and a 60% increase in the extinction at resonance. These trends are consistent with simulations performed using the discrete dipole approximation (DDA)⁴⁸ which indicate that these changes are more strongly

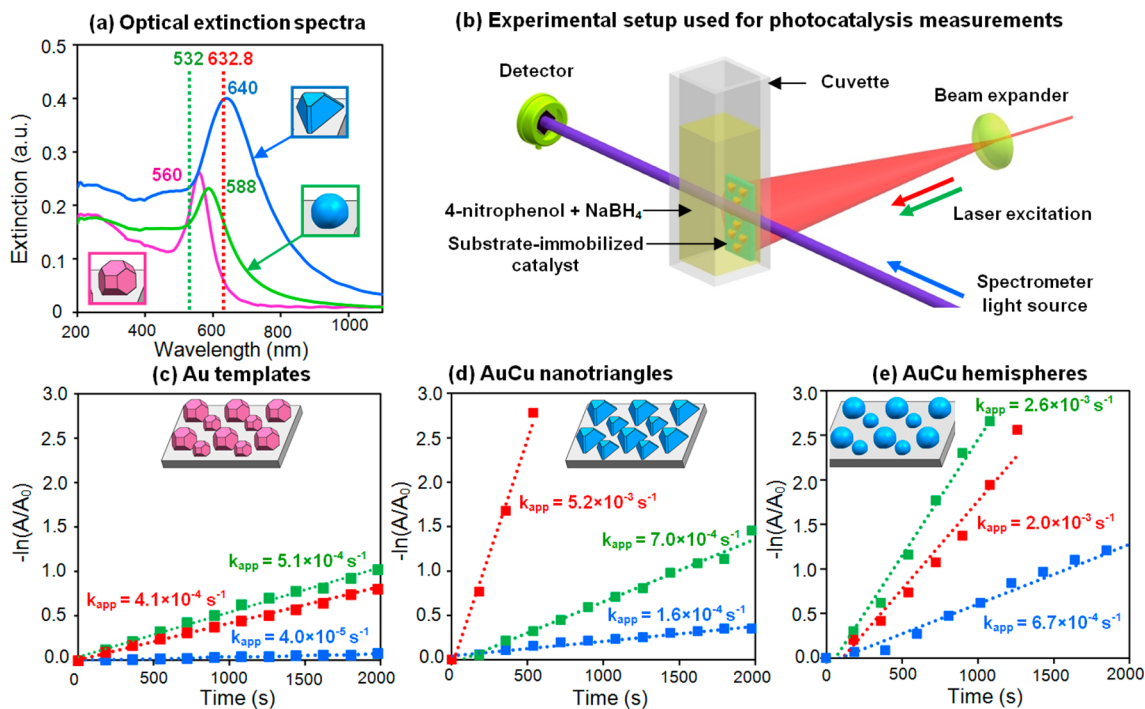


Figure 4. (a) Optical extinction spectra for Au templates (pink), AuCu triangular nanostructures (blue), and near-hemispherical AuCu nanostructures (green). The dashed red and green lines denote the laser excitation wavelengths used for photocatalysis. (b) Schematic representation of the experimental configuration used for photocatalysis measurements which sees the probe beam and the laser excitation source pass through the cuvette at right angles to each other. The time dependence of $-\ln(A/A_0)$ for (c) Au templates, (d) triangular AuCu nanostructures, and (e) near-hemispherical AuCu nanostructures where the blue, green, and red curves correspond to catalyst illumination under no light, green laser light, and red laser light, respectively. For all cases, the apparent reaction rate constant (k_{app}) derived from the slope is provided.

Table 1. Summary of Catalytic Descriptors for the Nanostructures Studied

nanostructure (composition)	laser	k_{app} (10^{-3} s^{-1}) ^a	$k_{app} \text{ mol}_{4\text{-AP}} \text{ g}^{-1}$ ($\mu\text{mol g}^{-1} \text{ s}^{-1}$) ^b	$k_{app} \text{ m}^{-2}$ ($\text{s}^{-1} \text{ m}^{-2}$)
triangular (AuCu)	red	5.2 ± 0.29	25	94
	green	0.70 ± 0.02	3.4	13
	none	0.16 ± 0.01	0.7	2.9
hemispherical (AuCu)	red	2.6 ± 0.18	13	65
	green	2.0 ± 0.14	9.8	50
	none	0.67 ± 0.03	3.3	17
Wulff shaped (Au)	red	0.41 ± 0.01	2.8	12
	green	0.51 ± 0.01	3.5	15
	none	0.041 ± 0.001	0.3	1.2

^aStandard deviations presented with 95% confidence intervals. ^bThe apparent rate constant multiplied by the number of moles of product per gram catalyst.

connected to the shape transformation than to Au–Cu alloying (Supporting Information, Figure S1).

Both the Au templates and the triangular AuCu nanostructures were evaluated as catalysts and photocatalysts using the model catalytic reaction which sees the reduction of 4-NP to 4-AP in the presence of sodium borohydride.⁴⁹ This reaction is typically preceded by a several minute induction period where the reaction is stalled until the catalytic particles become activated through a surface reconstruction.⁵⁰ All reactions utilized a 2 mL aqueous solution of 70 μM 4-NP and 7 mM NaBH_4 in a standard 1 cm path length quartz cuvette. The reaction was then initiated using a dip catalyst modality^{51,52} whereby the substrate-immobilized nanostructures are placed inside the cuvette such that it leans against one of its four sidewalls with the nanostructures facing the reactants as shown schematically in Figure 4b. This geometry has the advantage that it allows for the spectroscopic probe beam to pass through only the liquid reactants while allowing the laser beam, which is incident at a right angle to the probe beam, to pass sequentially through the sapphire substrate, the immobilized nanostructures and the reactants. In doing so, the probe beam is not compromised by interactions with the plasmonic nanoparticles. As is typical for this model catalytic reaction, we monitored the decrease in the 400 nm 4-NP absorption as it is reduced to 4-AP and then derive an apparent reaction rate constant, k_{app} , from the slope of the $\ln(A/A_0)$ vs time plot, where A/A_0 is the 4-NP absorbance normalized to its value at the end of the induction period.⁴⁹ Photocatalytic activity was promoted through the use of either a 532 nm green laser or a 632.8 nm red laser with an intensity of 10 mW/cm^2 .

Parts c and d of Figure 4 compare the catalytic and photocatalytic properties of the Au templates and the triangular AuCu nanostructures, respectively. For each case, k_{app} was determined when the nanostructures experienced no excitation and also when they were excited with red and green laser light. All of the data is plotted using the same upper bound on the y-axis to facilitate comparisons where the calculated reaction rate constants (i.e., k_{app}) are denoted next to each curve. Important to note is that the red and green laser wavelengths are near-coincident with the AuCu and Au LSPR peaks, respectively (denoted by the dashed lines in Figure 4a). A comparison of these catalysts under zero illumination reveals k_{app} values which are approximately 4 times greater for the triangular AuCu nanostructures, but where in both cases the reaction rate constants are one or 2 orders of magnitude lower than

competitive literature values.⁵³ This is somewhat expected considering the relatively large size of these nanostructures.⁵⁴ When illuminated, both Au and AuCu show improved rates. The Au templates show 10-fold and 13-fold enhancements under red and green illumination, respectively, where the larger value is achieved for the laser wavelength overlapping with the LSPR peak. Despite these enhancements, the values of k_{app} still remain uncompetitive with literature values. The same trends occur for the triangular AuCu nanostructures, showing a 4-fold enhancement for the off-resonant green laser and a 32-fold enhancement to k_{app} for the red laser resonant excitation. For this case, however, the k_{app} value of $5.2 \times 10^{-3} \text{ s}^{-1}$ is in-line with other high quality catalysts⁵³ and is an order magnitude higher than the Au values. When making such comparisons to the literature it should, however, be recognized that k_{app} values can be somewhat misleading since: (i) they are not normalized to the surface area or the quantity of catalyst used and (ii) they do not take into account the amount of product produced per second. Table 1 provides estimates of the moles of product produced per gram of catalyst per second and the reaction rate constants normalized to the surface area of the catalyst for all nanostructures used in this study. Comparison to literature values based on the latter metric (Supporting Information, Table S1) indicate that AuCu nanostructures are either competitive with or greatly exceed the values expressed by other Au, Cu and AuCu nanostructures. Of the structures examined, only AuCu nanorods²⁶ show a value which far exceeds the results reported here (ca. $500 \text{ s}^{-1} \text{ m}^{-2}$).

The wavelength dependence of the reaction rate constants for both the Au and AuCu nanostructures strongly suggests that the reduction of 4-NP can be enhanced through plasmonic photocatalysis. To further confirm this conclusion the triangular nanostructures used in Figure 4d were reheated to 750 °C for 90 min in the absence of Cu foil, a procedure which modifies the shape while maintaining the same composition and density of structures (Supporting Information, Figure S2). After this procedure the structures are near-hemispherical with an average diameter of approximately 100 nm. The shape transformation red-shifts the LSPR to 588 nm, a value which places it midway between the red and green laser excitation frequencies (Figure 4a). When the same photocatalytic measurements are performed on these structures (Figure 4e) the enhancements under red and green illumination are nearly identical as is expected for plasmonic photocatalysis. Beyond this determination, there are several other findings of significance derived

from this investigation: (i) a definitive determination that the reaction is proceeding through heterogeneous catalysis was made by simply removing the dip catalysts from the cuvette midway through the reaction and seeing the reaction halt (Supporting Information, Figure S3) and (ii) that, in addition to the reduction of 4-NP, all photocatalytic measurements resulted in the evolution of gas bubbles in quantities which correlate with the value of k_{app} for the reduction of 4-NP. It is noted that hydrogen gas evolution has been observed previously for this reaction when using heterogeneous catalysts.⁵³

The current study demonstrates that the reduction of 4-NP can be significantly enhanced if the LSPR of the catalytic nanostructures is excited with light. While no comparisons are currently available in the literature, this finding is consistent with the observation of plasmonic photocatalysis of the closely related compound 4-nitrothiophenol (4-NTP) as well as other nitroaromatics.^{55–59} While further study is required to pinpoint the exact dependence of the plasmonic enhancement on such factors as (i) the degree of alloying, (ii) the nanostructure shape, and (iii) the LSPR wavelength and extinction efficiency, it is possible to make some broad statements regarding the plasmonic photocatalysis of 4-NP to 4-AP. The fact that k_{app} is larger when the excitation wavelength is coincident with the LSPR is strongly supportive of the conclusion that plasmonic photocatalysis is responsible for the higher reaction rates when the sample is illuminated. Plasmonic photocatalysis is often associated with the interactions between plasmonic nanostructures and an active support (typically TiO_2) which participates in the reaction.^{31–34} This, however, is unlikely the case in the current study since it is improbable that the insulating sapphire substrate is participating in the catalytic reaction. It should be recognized, however, that the sapphire support can play an indirect role in that (i) it red-shifts the position of the LSPR peak and (ii) its high thermal conductivity (35 W/m·K) will reduce the potential influences of plasmon-induced heating on the catalysis process. From a mechanistic standpoint, the fact that the substrate is not directly participating in the catalytic response greatly simplifies the current situation as the plasmonic enhancement by the AuCu nanostructures must originate from the near-fields associated with the LSPR, hot electrons and/or the localized heating generated by plasmon decay.³² If the nanostructure heating is the sole source of the enhancement then, based on Arrhenius behavior⁵⁰ and an estimated activation energy of 1 eV for AuCu,⁶⁰ then a 32-fold increase in catalytic activity would require a temperature change of 29 °C.

In terms of nanostructure composition, the AuCu structures show superior catalytic and photocatalytic activity compared to Au where the superior activity is far beyond that which can be explained by the somewhat larger surface area expressed by the AuCu structures (see Table 1). It is not uncommon for bimetallic nanostructures to exhibit catalytic activity which exceeds its constituent components. Such behavior is often reconciled in terms of a volcano plot which shows that optimum catalytic activity occurs for an alloy composition where adsorbate-catalyst bonding is sufficiently strong to bind the reactant, but not so strong as to inhibit the desorption of the reaction product. 4-NP is shown by Pozun et al.⁶⁰ to bind weakly to Au and strongly to Cu, but where the bimetallic composition of $\text{Au}_{0.5}\text{Cu}_{0.5}$ lies near the optimum value.

While the nanoparticle composition is a crucial factor in determining catalytic activity, the expressed faceting of the

bimetallic nanostructure seems to be of secondary importance. The geometry of a triangular nanostructure is dominated by (111) facets which are expected to show little catalytic activity. It is, therefore, likely that the smaller (100) or (110) facets represent the active sites since such surfaces have been deemed catalytic in other systems.^{61,62} It is also conceivable that catalytic activity is associated with the highly undercoordinated sites which occur where the sharp facets intersect.⁶³ Also working in favor of the triangular geometry is the large extinction exhibited by the LSPR peak and the potential impact which the plasmonic near-field concentration at the triangle corners has on photocatalytic activity. In contrast, the rounded morphology of the near-hemispherical AuCu nanostructures must give rise to many atomic steps which are considered favorable for catalysis. Nevertheless, the triangular nanostructures, which show the fastest reaction rate constants in this study, likely do so because this geometry yields a LSPR peak which is resonant with the red excitation wavelength. While the near-hemispherical AuCu structures show a 2-fold reduction in the reaction rate constant, it should be recognized that the excitation wavelength is somewhat off-resonance. These results are demonstrative of the compromises which must be made when engineering plasmonic photocatalysts.

3. CONCLUSIONS

In summary, we have devised a route for the synthesis of substrate-immobilized AuCu triangular nanostructures and demonstrated these structures as plasmonic photocatalysts for the reduction of 4-NP to 4-AP. Despite the fact that these structures have dimensions well in excess of those which show the most pronounced catalytic behavior, it is possible, through photocatalysis, to achieve reaction rates which are competitive. Comparisons made to truncated octahedrons of Au indicate that the bimetallic nature of both the triangular AuCu nanostructures and near-hemispherical nanostructures is conducive to higher rates of reaction. In contrast to catalysis, where emphasis is placed on maximizing the number of catalytically active sites, these findings reveal that the maximization of photocatalytic enhancements to the reduction of 4-NP will require a cooperative balance between the (i) formation of active sites, (ii) the size of nanostructure, (iii) its chemical composition, and (iv) the plasmonic resonance and associated near-fields. Moreover, the study demonstrates the possibility of assessing the photocatalytic properties of plasmonic nanostructures using the reduction of 4-NP as a model catalytic reaction.

4. MATERIALS AND METHODS

Reagents and Chemicals. Triangular AuCu nanostructure synthesis utilized a Au sputter target cut from 0.5 mm thick foil with 99.9985% purity (Alfa Aesar), 0.0125 mm thick Cu foils with 99.9% purity, (0001)-oriented sapphire substrates (MTI Corp.), and ultrahigh purity Ar gas. Solutions for catalysis were prepared using 4-NP (Fluka), NaBH_4 (Fluka), and ultrapure deionized (DI) water (18.2 M Ω -cm at 25 °C). All chemicals were used as received.

AuCu Nanostructure Synthesis. The substrate-immobilized Au templates were formed through the solid-state dewetting of 12 nm thick sputter deposited films using procedures described in detail elsewhere.⁴¹ These films were deposited onto rectangular shaped (0001)-oriented sapphire substrates with dimensions of 6.5 mm \times 14 mm \times 0.5 mm. The

substrate and a Cu foil, with the same areal dimensions as the substrate, were then placed into adjacent slots cut into an alumina crucible (Figure 1b) where the separation distance is 0.5 mm. Prior to use, the foil was heated to 925 °C in flowing Ar (60 sccm) for 15 h, a procedure which proved crucial to the formation of a triangular geometry. While the need for this procedure remains unclear, we speculate that it not only removes the native oxide layer (as is indicated by a color change), but also sublimates volatile impurities contained within the 99.9% purity Cu foil which, in low concentrations, are detrimental to the assembly process. The loaded crucible is then inserted into a tube furnace with a flowing Ar ambient and exposed to a heating regimen which (i) ramps the temperature to 885 °C in 30 min, (ii) maintains this temperature for time intervals lasting up to 24 h and (iii) cools the sample to room temperature over the course of 2 h. The near-hemispherical 100 nm diameter AuCu nanostructures used in the catalysis measurements for comparison purposes was produced by reheating the triangular nanostructures to 750 °C for 90 min in the absence of a Cu foil. This procedure modifies the shape while maintaining the composition and density of the structures.

Catalysis. All catalysis measurements were performed using a 2 mL aqueous solution of 70 μ M 4-NP and 7 mM NaBH₄ prepared using DI water. The NaBH₄ was prepared fresh prior to each experiment and reacted within 2 min. The solution was loaded into a 1 cm path length quartz cuvette and the catalytic reaction was initiated by inserting the substrate into the solution such that its placement did not obstruct the spectroscopic probe beam. Catalytic activity was then monitored using UV–vis spectroscopy. For the case of photocatalytic experiments, the catalysts were exposed to repeated cycles where they were: (i) illuminated with either a red ($\lambda = 632.8$ nm) or green ($\lambda = 532$ nm) laser for a set time interval (typically 3 min) in an enclosure which blocked ambient light, (ii) removed from the enclosure and placed in the spectrometer where the UV–vis spectra was recorded and (iii) removed from the spectrometer where they were, once again, exposed to laser light. SEM characterization carried out after samples had undergone numerous reactions with and without laser irradiation showed no evidence of nanostructure degradation.

Instrumentation. A Model 681 Gatan High Resolution Ion Beam Coater was used to deposit ultrathin layers of Au onto sapphire substrates using a beam energy of 6 keV and measured penning gun currents of 200 μ A. The AuCu nanostructure assembly processes were carried out in a Lindberg Blue M tube furnace equipped with a quartz tube (outer diameter = 2.5 cm, length = 91 cm) and the required fittings to maintain a continuous flow of Ar gas. SEM images and EDS measurements were acquired using a FEI Quanta 450 FEG SEM environmental scanning electron microscope. The SEM images were taken in secondary electron mode with a beam energy of 30 kV. Side-view images were taken with the stage tilted at 45°. The images were processed to obtain histograms of the nanostructure dimensions using the ImageJ software package. EDS measurements were taken at a working distance of 10 nm, a beam spot size of 4.0 nm, and a beam energy of 30 kV. X-ray diffraction measurements utilized a Bruker D8 Discover X-ray diffractometer. The θ -2 θ scans were carried out using CuK α radiation at 2 θ intervals of 0.005° with collection times of 5 s. Optical spectra were obtained using a Jasco UV/vis Spectrophotometer V650. The extinction spectra were

collected at $\Delta\lambda$ intervals of 0.2 nm and used a sapphire substrate as a reference. The absorbance measurements used to obtain k_{app} were similarly carried out, but where a water baseline was used.

■ ASSOCIATED CONTENT

📄 Supporting Information

(i) DDA simulations of the expected LSPR peak for all structures studied as well as a description of the computation methods used to obtain the simulated results, (ii) SEM images, EDS maps, and XRD measurements performed on the near-hemispherical AuCu nanostructures which were used for comparative purposes in the photocatalysis measurements, (iii) catalysis data demonstrating that photocatalysis proceeds via heterogeneous catalysis, (iv) comparisons to literature k_{app} values when normalized to the surface area of the catalyst. The Supporting Information is available free of charge on the ACS Publications website at DOI: 10.1021/acs.jpcc.5b04618.

■ AUTHOR INFORMATION

Corresponding Author

*(S.N.) E-mail: neretina@temple.edu. Telephone 215-204-6326.

Notes

The authors declare no competing financial interest.

■ ACKNOWLEDGMENTS

This work is funded by the National Science Foundation (DMR-1053416) CAREER Award to S. Neretina. The authors also acknowledge the expertise of D. Dikin (Facility Manager, Nano Instrumentation Center, Temple University). The work has benefited from the facilities available through Temple University's Material Research Facility (MRF). K.D.G. acknowledges support received through a Temple University Graduate Student Fellowship.

■ REFERENCES

- (1) Liu, X. W.; Wang, D. S.; Li, Y. D. Synthesis and Catalytic Properties of Bimetallic Nanomaterials with various Architectures. *Nano Today* **2012**, *7*, 448–466.
- (2) Ferrando, R.; Jellinek, J.; Johnston, R. L. Nanoalloys: From Theory to Applications of Alloy Clusters and Nanoparticles. *Chem. Rev.* **2008**, *108*, 845–910.
- (3) Neațu, Ș.; Maciáa-Agulló, J. A.; Concepción, P.; Garcia, H. Gold–Copper Nanoalloys Supported on TiO₂ as Photocatalysts for CO₂ Reduction by Water. *J. Am. Chem. Soc.* **2014**, *136*, 15969–15976.
- (4) He, R.; Wang, Y.-C.; Wang, X.; Wang, Z.; Liu, G.; Zhou, W.; Wen, L.; Li, Q.; Wang, X.; Chen, X.; Zeng, J.; Hou, J. G. Facile Synthesis of Pentacle Gold–Copper Alloy Nanocrystals and their Plasmonic and Catalytic Properties. *Nat. Commun.* **2014**, *5*, 4327.
- (5) Hong, J. W.; Kang, S. W.; Choi, B.-S.; Kim, D.; Lee, S. B.; Han, S. W. Controlled Synthesis of Pd–Pt Alloy Hollow Nanostructures with Enhanced Catalytic Activities for Oxygen Reduction. *ACS Nano* **2012**, *6*, 2410–2419.
- (6) Cui, C.; Yu, J.; Li, H.; Gao, M.; Liang, H.; Yu, S. Remarkable Enhancement of Electrocatalytic Activity by Tuning the Interface of Pd–Au Bimetallic Nanoparticle Tubes. *ACS Nano* **2011**, *5*, 4211–4218.
- (7) Cortie, M. B.; McDonagh, A. M. Synthesis and Optical Properties of Hybrid and Alloy Plasmonic Nanoparticles. *Chem. Rev.* **2011**, *111*, 3713–3735.
- (8) Yang, Y.; Zhang, Q.; Fu, Z.-W.; Qin, D. Transformation of Ag Nanocubes into Ag–Au Hollow Nanostructures with Enriched Ag Contents to Improve SERS Activity and Chemical Stability. *ACS Appl. Mater. Interfaces* **2014**, *6*, 3750–3757.

- (9) Hao, R.; Xing, R. J.; Xu, Z. C.; Hou, Y. L.; Gao, S.; Sun, S. H. Synthesis, Functionalization, and Biomedical Applications of Multifunctional Magnetic Nanoparticles. *Adv. Mater.* **2010**, *22*, 2729–2742.
- (10) Bracey, C. L.; Ellis, P. R.; Hutchings, G. J. Applications of Copper-Gold Alloys in Catalysis: Current Status and Future Perspectives. *Chem. Soc. Rev.* **2009**, *38*, 2231–2243.
- (11) Hvolbæk, B.; Janssens, T. V. W.; Clausen, B. S.; Falsig, H.; Christensen, C. H.; Nørskov, J. K. Catalytic Activity of Au Nanoparticles. *Nano Today* **2007**, *2*, 14–18.
- (12) Behrens, M.; Studt, F.; Kasatkin, I.; Kühn, S.; Hävecker, M.; Abild-Pedersen, F.; Zander, S.; Girgsdies, F.; Kurr, P.; Knief, B.-L.; et al. The Active Site of Methanol Synthesis over Cu/ZnO/Al₂O₃ Industrial Catalysts. *Science* **2012**, *336*, 893–897.
- (13) Yin, A.; Wen, C.; Dai, W.-L.; Fan, K. Nanocasting of CuAu Alloy Nanoparticles for Methyl Glycolate Synthesis. *J. Mater. Chem.* **2011**, *21*, 8997–8999.
- (14) Yin, J.; Shan, S.; Yang, L.; Mott, D.; Malis, O.; Petkov, V.; Cai, F.; Ng, M. S.; Luo, J.; Chen, B. H.; et al. Gold-Copper Nanoparticles: Nanostructural Evolution and Bifunctional Catalytic Sites. *Chem. Mater.* **2012**, *24*, 4662–4674.
- (15) Liu, X. Y.; Wang, A. Q.; Wang, X. D.; Mou, C. Y.; Zhang, T. Au-Cu Alloy Nanoparticles Confined in SBA-15 as a Highly Efficient Catalyst for CO Oxidation. *Chem. Commun.* **2008**, *27*, 3187–3189.
- (16) Pina, C. D.; Falletta, E.; Rossi, M. Highly Selective Oxidation of Benzyl Alcohol to Benzaldehyde Catalyzed by Bimetallic Gold-Copper Catalyst. *J. Catal.* **2008**, *260*, 384–386.
- (17) Llorca, J.; Domínguez, M.; Ledesma, C.; Chimentão, R. J.; Medina, F.; Sueiras, J.; Angurell, I.; Seco, M.; Rossell, O. Propene Epoxidation Over TiO₂-Supported Au-Cu Alloy Catalysts Prepared from Thiol-Capped Nanoparticles. *J. Catal.* **2008**, *258*, 187–198.
- (18) Zhao, W.; Yang, L.; Yin, Y.; Jin, M. Thermodynamic Controlled Synthesis of Intermetallic Au₃Cu Alloy Nanocrystals from Cu Microparticles. *J. Mater. Chem. A* **2014**, *2*, 902–906.
- (19) Wang, C.; Astruc, D. Nanogold Plasmonic Photocatalysis for Organic Synthesis and Clean Energy Conversion. *Chem. Soc. Rev.* **2014**, *43*, 7188–7216.
- (20) Kim, D.; Resasco, J.; Yu, Y.; Asiri, A. M.; Yang, P. Synergistic Geometric and Electronic Effects for Electrochemical Reduction of Carbon Dioxide using Gold-Copper Bimetallic Nanoparticles. *Nat. Commun.* **2014**, *5*, 4948.
- (21) Najafshirvari, S.; Brescia, R.; Guardia, P.; Marras, S.; Manna, L.; Colombo, M. Nanoscale Transformations of Alumina-Supported AuCu Ordered Phase Nanocrystals and Their Activity in CO Oxidation. *ACS Catal.* **2015**, *5*, 2154–2163.
- (22) Sinha, S. K.; Srivastava, C.; Sampath, S.; Chattopadhyay, K. Tunability of Monodispersed Intermetallic AuCu Nanoparticles through Understanding of Reaction Pathways. *RSC Adv.* **2015**, *5*, 4389–4395.
- (23) Andolina, C. M.; Dewar, A. C.; Smith, A. M.; Marbella, L. E.; Hartmann, M. J.; Millstone, J. E. Photoluminescent Gold-Copper Nanoparticle Alloys with Composition-Tunable Near-Infrared Emission. *J. Am. Chem. Soc.* **2013**, *135*, 5266–5269.
- (24) Bauer, J. C.; Mullins, D.; Li, M.; Wu, Z.; Payzant, E. A.; Overbury, S. H.; Dai, S. Synthesis of Silica Supported AuCu Nanoparticle Catalysts and the Effects of Pretreatment Conditions for the CO Oxidation Reaction. *Phys. Chem. Chem. Phys.* **2011**, *13*, 2571–2581.
- (25) Sra, A. K.; Ewers, T. D.; Schaak, R. E. Direct Solution Synthesis of Intermetallic AuCu and AuCu₃ Nanocrystals and Nanowire Networks. *Chem. Mater.* **2005**, *17*, 758–766.
- (26) Chen, S.; Jenkins, S. V.; Tao, J.; Zhu, Y.; Chen, J. Anisotropic Seeded Growth of Cu-M (M = Au, Pt, or Pd) Bimetallic Nanorods with Tunable Optical and Catalytic Properties. *J. Phys. Chem. C* **2013**, *117*, 8924–8932.
- (27) Jiang, Z.; Zhang, Q.; Zong, C.; Liu, B.-J.; Ren, B.; Xie, Z.; Zheng, L. Cu-Au Alloy Nanotubes with Five-Fold Twinned Structure and Their Application in Surface-Enhanced Raman Scattering. *J. Mater. Chem.* **2012**, *22*, 18192–18197.
- (28) Liu, Y.; Walker, A. R. H. Monodisperse Gold-Copper Bimetallic Nanocubes: Facile One-Step Synthesis with Controllable Size and Composition. *Angew. Chem., Int. Ed.* **2010**, *49*, 6781–6785.
- (29) Henkel, A.; Jakab, A.; Brunklaus, G.; Sönnichsen, C. Tuning Plasmonic Properties by Alloying Copper into Gold Nanorods. *J. Phys. Chem. C* **2009**, *113*, 2200–2204.
- (30) Jing, H.; Zhang, Q.; Large, N.; Yu, C.; Blom, D. A.; Nordlander, P.; Wang, H. Tunable Plasmonic Nanoparticles with Catalytically Active High-Index Facets. *Nano Lett.* **2014**, *14*, 3674–3682.
- (31) Linic, S.; Aslam, U.; Boerigter, C.; Morabito, M. Photochemical Transformations on Plasmonic Metal Nanoparticles. *Nat. Mater.* **2015**, *14*, 567–576.
- (32) Zhang, X.; Chen, Y. L.; Liu, R.-S.; Tsai, D. P. Plasmonic Photocatalysis. *Rep. Prog. Phys.* **2013**, *76*, 046401.
- (33) Hou, W.; Cronin, S. B. A Review of Surface Plasmon Resonance-Enhanced Photocatalysis. *Adv. Funct. Mater.* **2013**, *23*, 1612–1619.
- (34) Christopher, P.; Xin, H.; Linic, S. Visible Light-Enhanced Catalytic Oxidation Reactions on Plasmonic Silver Nanostructures. *Nat. Chem.* **2011**, *3*, 467–472.
- (35) Gilroy, K. D.; Sundar, A.; Hajfathalian, M.; Yaghoobzade, A.; Tan, T.; Sil, D.; Borguet, E.; Hughes, R. A.; Neretina, S. Transformation of Truncated Gold Octahedrons into Triangular Nanoprisms through the Heterogeneous Nucleation of Silver. *Nanoscale* **2015**, *7*, 6827–6835.
- (36) Sundar, A.; Farzinpour, P.; Gilroy, K. D.; Tan, T.; Hughes, R. A.; Neretina, S. Eutectic Combinations as a Pathway to the Formation of Substrate-Based Au-Ge Heterodimers and Hollowed Au Nanocrescents with Tunable Optical Properties. *Small* **2014**, *10*, 3379–3388.
- (37) Sundar, A.; Farzinpour, P.; Gilroy, K. D.; Tan, T.; Hughes, R. A.; Neretina, S. Organized Surfaces of Highly Faceted Single-Crystal Palladium Structures Seeded by Sacrificial Templates. *Cryst. Growth Des.* **2013**, *13*, 3847–3851.
- (38) Sundar, A.; Hughes, R. A.; Farzinpour, P.; Gilroy, K. D.; Devenyi, G. A.; Preston, J. S.; Neretina, S. Manipulating the Size Distribution of Supported Gold Nanostructures. *Appl. Phys. Lett.* **2012**, *100*, 013111.
- (39) Millstone, J. E.; Hurst, S. J.; Métraux, G. S.; Cutler, J. I.; Mirkin, C. A. Colloidal Gold and Silver Triangular Nanoprisms. *Small* **2009**, *5*, 646–664.
- (40) Thompson, C. V. Solid-State Dewetting of Thin Films. *Annu. Rev. Mater. Res.* **2012**, *42*, 399–434.
- (41) Farzinpour, P.; Sundar, A.; Gilroy, K. D.; Eskin, Z. E.; Hughes, R. A.; Neretina, S. Altering the Dewetting Characteristics of Ultrathin Gold and Silver Films Using a Sacrificial Antimony Layer. *Nanotechnology* **2012**, *23*, 495604.
- (42) Jenkins, S. V.; Chen, S.; Chen, J. Gold-Copper Alloyed Nanorods for Metal-Catalyzed Organic Reactions: Implication of Surface Ligands on Nanoparticle-Based Heterogeneous Catalysis. *Tetrahedron Lett.* **2015**, *56*, 3368–3372.
- (43) Li, D.; Wang, C.; Tripkovic, D.; Sun, S.; Markovic, N. M.; Stamenkovic, V. R. Surfactant Removal for Colloidal Nanoparticles from Solution Synthesis: The Effect on Catalytic Performance. *ACS Catal.* **2012**, *2*, 1358–1362.
- (44) Zhang, Q.; Blom, D. A.; Wang, H. Nanoporosity-Enhanced Catalysis on Subwavelength Au Nanoparticles: A Plasmon-Enhanced Spectroscopic Study. *Chem. Mater.* **2014**, *26*, 5131–5142.
- (45) Henry, C. R. Morphology of Supported Nanoparticles. *Prog. Surf. Sci.* **2005**, *80*, 92–116.
- (46) Chatain, D.; Ghetta, V.; Wynblatt, P. Equilibrium Shape of Copper Crystals Grown on Sapphire. *Interface Sci.* **2004**, *12*, 7–18.
- (47) Okamoto, H.; Chakrabarti, D. J.; Laughlin, D. E.; Massalski, T. B. The Au-Cu (Gold-Copper) System. *J. Phase Equilib.* **1987**, *8*, 454–474.
- (48) Draine, B. T.; Flatau, P. J. Discrete-Dipole Approximation for Scattering Calculations. *J. Opt. Soc. Am. A* **1994**, *11*, 1491–1499.

(49) Hervés, P.; Pérez-Lorenzo, M.; Liz-Marzán, L. M.; Dzubiella, J.; Lu, Y.; Ballauff, M. Catalysis by Metallic Nanoparticles in Aqueous Solution: Model Reactions. *Chem. Soc. Rev.* **2012**, *41*, 5577–5587.

(50) Wunder, S.; Lu, Y.; Albrecht, M.; Ballauff, M. Catalytic Activity of Faceted Gold Nanoparticles Studied by a Model Reaction: Evidence for Substrate-Induced Surface Restructuring. *ACS Catal.* **2011**, *1*, 908–916.

(51) Zheng, G.; Polavarapu, L.; Liz-Marzán, L. M.; Pastoriza-Santos, I.; Pérez-Juste, J. Gold Nanoparticle-Loaded Filter Paper: A Recyclable Dip-Catalyst for Real-Time Monitoring by Surface Enhanced Raman Scattering. *Chem. Commun.* **2015**, *51*, 4572–4575.

(52) Hariprasad, E.; Radhakrishnan, T. P. A Highly Efficient and Extensively Reusable “Dip Catalyst” Based on a Silver-Nanoparticle-Embedded Polymer Thin Film. *Chem. - Eur. J.* **2010**, *16*, 14378–14384.

(53) Zhao, P.; Feng, X.; Huang, D.; Yang, G.; Astruc, D. Basic Concepts and Recent Advances in Nitrophenol Reduction by Gold- and Other Transition Metal Nanoparticles. *Coord. Chem. Rev.* **2015**, *287*, 114–136.

(54) Fenger, R.; Fertitta, E.; Kirmse, H.; Thünemann, A. F.; Rademann, K. Size Dependent Catalysis with CTAB-Stabilized Gold Nanoparticles. *Phys. Chem. Chem. Phys.* **2012**, *14*, 9343–9349.

(55) Fang, Y.; Li, Y.; Xu, H. X.; Sun, M. T. Ascertaining p,p'-Dimercaptoazobenzene Produced from p-Aminothiophenol by Selective Catalytic Coupling Reaction on Silver Nanoparticles. *Langmuir* **2010**, *26*, 7737–7746.

(56) Huang, Y.-F.; Zhu, H.-P.; Liu, G.-K.; Wu, D.-Y.; Ren, B.; Tian, Z.-Q. When the Signal Is Not from the Original Molecule To Be Detected: Chemical Transformation of para-Aminothiophenol on Ag during the SERS Measurement. *J. Am. Chem. Soc.* **2010**, *132*, 9244–9246.

(57) Sun, M. T.; Xu, H. X. A Novel Application of Plasmonics: Plasmon-Driven Surface-Catalyzed Reactions. *Small* **2012**, *8*, 2777–2786.

(58) Kim, K.; Choi, J.-Y.; Shin, K. S. Photoreduction of 4-Nitrobenzenethiol on Au by Hot Electrons Plasmonically Generated from Ag Nanoparticles: Gap-Mode Surface-Enhanced Raman Scattering Observation. *J. Phys. Chem. C* **2015**, *119*, 5187–5194.

(59) Zhu, H.; Ke, X.; Yang, X.; Sarina, S.; Liu, H. Reduction of Nitroaromatic Compounds on Supported Gold Nanoparticles by Visible and Ultraviolet Light. *Angew. Chem., Int. Ed.* **2010**, *49*, 9657–9661.

(60) Pozun, Z. D.; Rodenbusch, S. E.; Keller, E.; Tran, K.; Tang, W.; Stevenson, K. J.; Henkelman, G. A Systematic Investigation of p-Nitrophenol Reduction by Bimetallic Dendrimer Encapsulated Nanoparticles. *J. Phys. Chem. C* **2013**, *117*, 7598–7604.

(61) Zhang, Q.; Wang, H. Facet-Dependent Catalytic Activities of Au Nanoparticles Enclosed by High-Index Facets. *ACS Catal.* **2014**, *4*, 4027–4033.

(62) Eo, M.; Baek, J.; Song, H. D.; Lee, S.; Yi, J. Quantification of Electron Transfer Rates of Different Facets on Single Gold Nanoparticles during Catalytic Reactions. *Chem. Commun.* **2013**, *49*, 5204–5206.

(63) Mostafa, S.; Behafarid, F.; Croy, J. R.; Ono, L. K.; Li, L.; Yang, J. C.; Frenkel, A. I.; Cuenya, B. R. Shape-Dependent Catalytic Properties of Pt Nanoparticles. *J. Am. Chem. Soc.* **2010**, *132*, 15714–15719.